Shell and cluster states of $_{\Lambda}^{21}$Ne studied with antisymmetrized molecular dynamics

Masahiro Isaka,[1] Masaaki Kimura,[2] Akinobu Doté,[3] and Akira Ohnishi[4]

[1]*Department of Cosmosciences, Graduate School of Science, Hokkaido University, Sapporo 060-0810, Japan*
[2]*Creative Research Institution (CRIS), Hokkaido University, Sapporo 001-0021, Japan*
[3]*Institute of Particle and Nuclear Studies, KEK, Tsukuba, Ibaraki 305-0801, Japan*
[4]*Yukawa Institute for Theoretical Physics, Kyoto University, Kyoto 606-8502, Japan*

The low-lying states of $_{\Lambda}^{21}$Ne are studied with antisymmetrized molecular dynamics for hypernuclei. We have obtained ten rotational bands where the number of bands are increased compared to ^{20}Ne by adding a Λ hyperon. Among them, we focus on the $K^{\pi} = 0_1^+ \otimes \Lambda_s$ and $K^{\pi} = 0_1^- \otimes \Lambda_s$ bands. The former has a shell-model-like structure that has Λ in an s wave coupled to the ground band of ^{20}Ne. The latter is a cluster state that has a $\alpha + _{\Lambda}^{17}$O dicluster structure. The difference between their structures leads to the binding energy of Λ particle B_{Λ} and reduction of the $E2$ transition probabilities $B(E2)$.

I. INTRODUCTION

One of the unique and interesting aspects of hypernuclei is structure changes caused by hyperons. Experimental and theoretical studies have revealed a couple of interesting structure changes in p-shell Λ hypernuclei [1–9]. For example, the reduction of the intercluster distance due to the attraction by a Λ hyperon has been confirmed through the observation of $E2$ transition probabilities $B(E2)$ in $_{\Lambda}^{7}$Li [1,5,10,11], that has developed an $\alpha + d + \Lambda$ cluster structure. In sd-shell Λ hypernuclei, various structure changes will occur depending on the structure of the core nuclei, since sd-shell normal nuclei have various structures in ground and low-energy states [12–14]. For example, the parity inversion of the $_{\Lambda}^{20}$Ne ground state was predicted [15]. In $_{\Lambda}^{21}$Ne, the stabilization of the unbound $\alpha + {}^{16}$O cluster states and the reduction of $B(E2)$ due to the shrinkage of the intercluster distance were discussed [16].

In the last decade, our knowledge of ΛN interaction has greatly increased. By both theoretical and experimental efforts, most of the central part of a ΛN effective interaction has been clarified [2,17–23]. This makes it possible to investigate the structure of various Λ hypernuclei systematically and quantitatively by using these ΛN interactions. Adding to this, in the study of unstable nuclei, theoretical models without any assumption on nuclear structure have been developed. As a typical example of such theoretical models, antisymmetrized molecular dynamics (AMD) has been successful in describing various structures of neutron-rich p-sd shell nuclei [24–28]. Therefore, we suggest AMD as a powerful tool for the study of hypernuclear structure [29] by using effective ΛN interactions.

In this paper, we have applied an extended version of AMD for hypernuclei (HyperAMD) to $_{\Lambda}^{21}$Ne and investigated its structure. ^{20}Ne is a typical nucleus having various structures within a small excitation energy region. The ground band and $K^{\pi} = 0_1^-$ band built on the 1_1^- state at 5.79 MeV constitute the parity doublet associated with $\alpha + {}^{16}$O clustering. It is known that the $K^{\pi} = 0_1^-$ band has the pronounced $\alpha + {}^{16}$O clustering, while the ground band has the mixing between the deformed shell structure and $\alpha + {}^{16}$O cluster structure [12,13,28]. In addition to these, the $K^{\pi} = 2_1^-$ band with a deformed shell-model-like structure is built on the 2_1^- state at 4.97 MeV. Therefore, it is of interest to investigate how a Λ hyperon will affect and modify their structures. We have found that a Λ hyperon in s and p orbits, respectively, generate five bands each. Among them, in this paper, we focus on the $K^{\pi} = 0_1^+ \otimes \Lambda_s$ and $K^{\pi} = 0_1^- \otimes \Lambda_s$ bands. The former has a shell-model-like structure where Λ in an s wave is coupled to the ground band of ^{20}Ne. The latter is a cluster state that has $\alpha + _{\Lambda}^{17}$O dicluster structure. The $K^{\pi} = 0_1^- \otimes \Lambda_s$ band is bound due to the "gluelike role" of the Λ hyperon. The differences in their structures lead to the difference in the binding energy of the Λ hyperon B_{Λ} and the magnitude of the $B(E2)$ reduction.

This paper is organized as follows. In the next section, we explain the theoretical framework of HyperAMD. In the Sec. III, the low-lying states of $_{\Lambda}^{21}$Ne and their properties are discussed. The differences between shell and cluster states are the focus. The final section summarizes this work.

II. FRAMEWORK

In this study, we have applied an extended version of AMD for hypernuclei (HyperAMD) to $_{\Lambda}^{21}$Ne. In this study, we also describe the single Λ hypernuclei; and a ΛN-ΣN coupling is not included in the model space.

A. Wave function

The single Λ hypernucleus composed of A nucleons and a Λ hyperon is described by the wave function that is an eigenstate of the parity,

$$\Psi^{\pm} = \hat{P}^{\pm}\Psi_{\text{int}}, \tag{1}$$

where $\hat{P}^{\pm}$ is the parity projector and the intrinsic wave function Ψ_{int} is represented by the direct product of the Λ single-particle wave function φ_{Λ} and the wave function of A nucleons Ψ_N,

$$\Psi_{\text{int}} = \varphi_{\Lambda} \otimes \Psi_N. \tag{2}$$

The nuclear part is described by a Slater determinant of nucleon single-particle wave packets,

$$\Psi_N = \frac{1}{\sqrt{A!}} \det\{\psi_i(r_j)\}, \tag{3}$$

$$\psi_i(r_j) = \phi_i(r_j)\chi_i\eta_i, \tag{4}$$

$$\phi_i(r) = \prod_{\sigma=x,y,z} \left(\frac{2\nu_\sigma}{\pi}\right)^{1/4} \exp\{-\nu_\sigma(r - Z_i)^2_\sigma\}, \tag{5}$$

$$\chi_i = \alpha_i\chi_\uparrow + \beta_i\chi_\downarrow, \tag{6}$$

$$\eta_i = \text{proton or neutron}, \tag{7}$$

where ψ_i is ith nucleon single-particle wave packet consisting of spatial ϕ_i, spin χ_i, and isospin η_i parts. The spatial part ϕ_i is represented by a deformed Gaussian. Its centroid $\mathbf{Z}_i$ is a complex three-dimensional vector. The width parameters ν_σ are real numbers and take independent values for each direction, but are common to all nucleons. The spin part is parameterized by the complex parameters α_i and β_i, and the isospin part is fixed to a proton or neutron. $\mathbf{Z}_i$, ν_σ, α_i, and β_i are the variational parameters of the nuclear part.

To describe various orbits of the Λ hyperon, the Λ single-particle wave function is represented by the superposition of Gaussian wave packets,

$$\varphi_\Lambda(r) = \sum_{m=1}^M c_m\varphi_m(r), \quad \varphi_m(r) = \phi_m(r)\chi_m, \tag{8}$$

$$\phi_m(r) = \prod_{\sigma=x,y,z} \left(\frac{2\nu_\sigma\mu}{\pi}\right)^{1/4} \exp\{-\nu_\sigma\mu(r - z_m)^2_\sigma\}, \tag{9}$$

$$\chi_m = a_m\chi_\uparrow + b_m\chi_\downarrow, \tag{10}$$

$$\mu = \frac{m_\Lambda}{m_N}, \tag{11}$$

where m_Λ and m_N represent the masses of the Λ particle and the nucleon, respectively. Again, each wave packet is parametrized by the centroid of Gaussian $\mathbf{z}_m$, and the spin direction a_m and b_m. The terms $\mathbf{z}_m$, a_m, b_m, and c_m are the variational parameters of the hyperon part.

Those variational parameters of nuclear and hyperon parts are optimized through the frictional cooling method described below. The number of basis wave packets M is so chosen that the variational calculation is sufficiently converged.

B. Hamiltonian and constraints

The Hamiltonian used in this study is given as

$$\hat{H} = \hat{T}_N + \hat{T}_\Lambda - \hat{T}_g + \hat{V}_{NN} + \hat{V}_{\Lambda N} + \hat{V}_{\text{Coul}}. \tag{12}$$

Here, $\hat{T}_N$, $\hat{T}_\Lambda$, and $\hat{T}_g$ are the kinetic energies of nucleons, a Λ hyperon, and the center-of-mass motion. Since we have superposed Gaussian wave packets to describe the Λ single-particle wave function, it is rather tedious to remove the spurious center-of-mass kinetic energy exactly. To reduce it, we keep the center of mass of wave packets at the origin of the coordinate:

$$\sum_{i=1}^A \mathbf{Z}_i + \sum_{m=1}^M \sqrt{\mu}\mathbf{z}_m = 0. \tag{13}$$

We expect that the spurious energy is not large in sd-shell hypernuclei, because the number of nucleons is much larger than the s- or p-shell hypernuclei.

Our model wave function is designed to describe the low-momentum phenomena as in the conventional shell model, and

we shall use the low-momentum effective interaction. We have used the Gogny D1S interaction [30] as an effective nucleon-nucleon interaction $\hat{V}_{NN}$, that has been successfully applied to the stable and unstable normal nuclei. As an effective ΛN interaction, we have used the central part of the ND version of YNG (YNG-ND) interaction [23]. The Coulomb interaction is approximated by the sum of seven Gaussians.

We have imposed two constraints on the variational calculation. The first is on the nuclear quadrupole deformation parameter β that is achieved by adding the parabolic potential

$$\langle\hat{V}_\beta\rangle = v_\beta(\beta - \beta_0)^2 \tag{14}$$

to the total energy. Here, β denotes the quadrupole deformation of the nuclear wave function Ψ_N whose definition is given in Ref. [25]. The value of v_β is chosen large enough that the deformation of Ψ_N is equal to β_0 after the variation. It is noted that there are no constraints on the nuclear quadrupole deformation γ and the deformation of the Λ single-particle oribtal. They have optimum values after the variational calculation for each given value of β_0.

Another constraint is on the Λ single-particle orbit by adding the potential,

$$\hat{V}_s = \lambda|\varphi_s\rangle\langle\varphi_s|, \tag{15}$$

$$\langle\mathbf{r}|\varphi_s\rangle = \exp[-\mu\bar{\nu}r^2], \tag{16}$$

$$\bar{\nu} = 3\sqrt{\nu_x\nu_y\nu_z} \tag{17}$$

to the Hamiltonian. Here, φ_s describes the wave function of a Λ hyperon in an s orbit as a Gaussian wave packet at the origin of the coordinate. By applying a sufficiently large value to λ, this potential forbids the Λ in an s wave. Therefore, by switching off and on this potential, we, respectively, obtain the hypernuclear states where a Λ hyperon occupies s and p waves. We shall denote the former state as Λ_s and the latter one as Λ_p.

The total energy plus constraint potentials,

$$E' = \frac{\langle\Psi^\pm|\hat{H}|\Psi^\pm\rangle}{\langle\Psi^\pm|\Psi^\pm\rangle} + \frac{\langle\Psi^\pm|\hat{V}_s|\Psi^\pm\rangle}{\langle\Psi^\pm|\Psi^\pm\rangle} + \langle V_\beta\rangle, \tag{18}$$

is minimized through the frictional cooling method. The imaginary time development equations of the variational parameters are given as

$$\frac{dX_i}{dt} = \frac{\kappa}{\hbar}\frac{\partial E'}{\partial X_i^*}, \tag{19}$$

$$X_i = \mathbf{Z}_i, \mathbf{z}_i, \alpha_i, \beta_i, a_i, b_i, \nu_i, \tag{20}$$

where κ is arbitrary negative real number. Finally, we obtain hypernuclear states with Λ_s and $\Psi_s(\beta_0)$, or Λ_p and $\Psi_p(\beta_0)$, for each β_0.

C. Angular momentum projection and the generator coordinate method (GCM)

From the optimized wave function, we project out the eigenstate of the total angular momentum J,

$$\Psi^{J\pm}_{s\text{ or }p,MK}(\beta_0) = \hat{P}^{J\pm}_{MK}\Psi_{s\text{ or }p}(\beta_0). \tag{21}$$

Here, $\hat{P}_{MK}^{J\pm}$ is a total angular momentum and parity projector. The integrals over three Euler angles included in the $\hat{P}_{MK}^{J\pm}$ are evaluated by numerical integration.

Finally, we superpose the wave functions $\Psi_{sMK}^{J\pm}(\beta_0)$ and $\Psi_{pMK}^{J\pm}(\beta_0)$ which have the same parity and angular momentum but have different values of the deformation parameter β_0 and K (generator coordinate method). Thus, the final wave function of the system becomes as follows:

$$\Psi_n^{J\pm} = c_{1n}\Psi_{sMK}^{J\pm}(\beta_0) + c_{2n}\Psi_{sMK'}^{J\pm}(\beta_0')$$
$$+ \cdots + c_{1n}'\Psi_{pMK}^{J\pm}(\beta_0) + c_{2n}'\Psi_{pMK'}^{J\pm}(\beta_0') + \cdots,$$

where quantum numbers other than total angular momentum and parity are represented by n. The coefficients $c_{1n}, c_{1n}', c_{2n}, c_{2n}', \ldots$ are determined by the following equation:

$$\delta\left(\left\langle\Psi_n^{J\pm}\left|\hat{H}\right|\Psi_n^{J\pm}\right\rangle - \epsilon_n\left\langle\Psi_n^{J\pm}\middle|\Psi_n^{J\pm}\right\rangle\right) = 0. \quad (22)$$

The GCM amplitude describes the contributions from the AMD wave functions having various β to the resulting GCM ones defined as in Eq. (22). The GCM amplitude is defined as follows:

$$\left|C_n^{J\pm}(\beta_0)\right|^2 = \left|\left\langle\Psi_n^{J\pm}\middle|\Psi_{s\;\text{or}\;p,MK}^{J\pm}(\beta_0)\right\rangle\right|^2. \quad (23)$$

As we shall discuss latter, the GCM amplitude is useful for analyzing the mixing of wave functions with the other configurations.

Using the GCM wave functions given in Eq. (22), we calculate the expectation values of Λ kinetic energy T_Λ and ΛN potential energy $V_{\Lambda N}$. In addition, we define the E_N as the residual energy of the system:

$$E_N = B({}^{21}_{\Lambda}\text{Ne}(J^\pi)) - (T_\Lambda + V_{\Lambda N}), \quad (24)$$

describing dominantly the expectation values of the operators $\hat{T}_N + \hat{V}_{NN} + \hat{V}_{\text{Coul}}$ in the hypernucleus. Here, $B({}^{21}_{\Lambda}\text{Ne})$ denotes the binding energy of the J^π state in ${}^{21}_{\Lambda}$Ne.

D. Λ binding energy

To analyze the dependence of Λ binding energy on the core structure, we define the Λ binding energy B_Λ in a hypernucleus. According to our calculation, it is found that the hypernuclear state $\Psi_{s\;\text{or}\;p}^{J\pm}$ is well described as

$$\Psi_{s\;\text{or}\;p}^{J\pm} \simeq [\Psi_N(j^\pi) \otimes \varphi_\Lambda(s\;\text{or}\;p)]_{J\pm}. \quad (25)$$

Thus, we define B_Λ as follows:

$$B_\Lambda = B({}^{21}_{\Lambda}\text{Ne}(J^\pi)) - B({}^{20}\text{Ne}(j^\pi)). \quad (26)$$

Here, $B({}^{20}\text{Ne}(j^\pi))$ and $B({}^{21}_{\Lambda}\text{Ne}(J^\pi))$ represent the binding energies of the j^π state of ^{20}Ne and of the J^π state of ${}^{21}_{\Lambda}$Ne, respectively.

III. RESULTS

A. Energy spectra of ^{20}Ne

The calculated and observed low-lying energy spectrum of ^{20}Ne is presented in Fig. 1. After the GCM calculation, the AMD describes successfully the ground band ($K^\pi = 0_1^+$), the
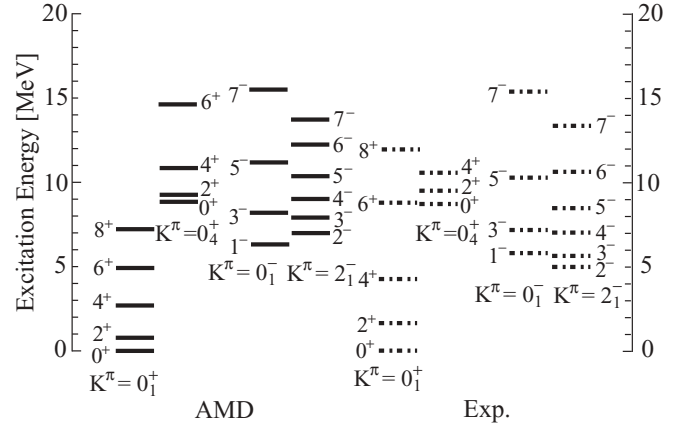
FIG. 1. Low-lying energy spectra of ^{20}Ne obtained with AMD. For comparison, corresponding experimental data are also presented.

$K^\pi = 0_4^+$ band which is the higher nodal band, the $K^\pi = 0_1^-$ band, and the $K^\pi = 2_1^-$ band. The $K^\pi = 0_1^-$ band is a parity doublet partner of the ground band with the pronounced $\alpha + {}^{16}$O cluster structure. The mixing between mean-field and cluster structures in the ground band has been discussed [28,31,32]. In Figs. 2(a)–2(c), the intrinsic density distributions of the band head states of ^{20}Ne are presented. It shows the prominent $\alpha + {}^{16}$O clustering of the $K^\pi = 0_1^-$ band and the shell-model-like nature of the $K^\pi = 2_1^-$ band. The ground band has mixed nature between the $\alpha + {}^{16}$O cluster and the $(sd)^4$ shell structure.

B. ${}^{21}_{\Lambda}$Ne hypernucleus

1. Energy spectra of ${}^{21}_{\Lambda}$Ne

In ${}^{21}_{\Lambda}$Ne, Λ hyperon coupled to ^{20}Ne generates ten bands. These bands can be classified into two groups. The former five bands have Λ_s, while the latter five bands have Λ_p.

The energy spectra of ${}^{21}_{\Lambda}$Ne with Λ_s are shown in Fig. 3. These are five bands corresponding to the $K^\pi = 0_1^+, 0_4^+, 0_1^-, 0_2^-$, and 2_1^- bands of ^{20}Ne. We call them, respectively, the $0_1^+ \otimes \Lambda_s$ (0_1^+ band with Λ_s), $0_4^+ \otimes \Lambda_s$, $0_1^- \otimes \Lambda_s$, $0_2^- \otimes \Lambda_s$, and $2_1^- \otimes \Lambda_s$ bands. In Fig. 3, the experimental ^{20}Ne $+ \Lambda$ and
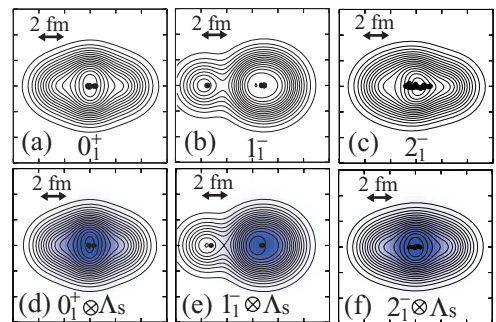
FIG. 2. (Color online) (a)–(c) Density distributions of the band head states of the $K^\pi = 0_1^+$, $K^\pi = 0_1^-$ and $K^\pi = 2_1^-$ bands in ^{20}Ne. (d)–(f) Corresponding states with Λ_s in ${}^{21}_{\Lambda}$Ne. The solid lines show the nucleon density, while the color plot shows the density distribution of the Λ hyperon. The closed circles show the centroids of nucleon wave packets.
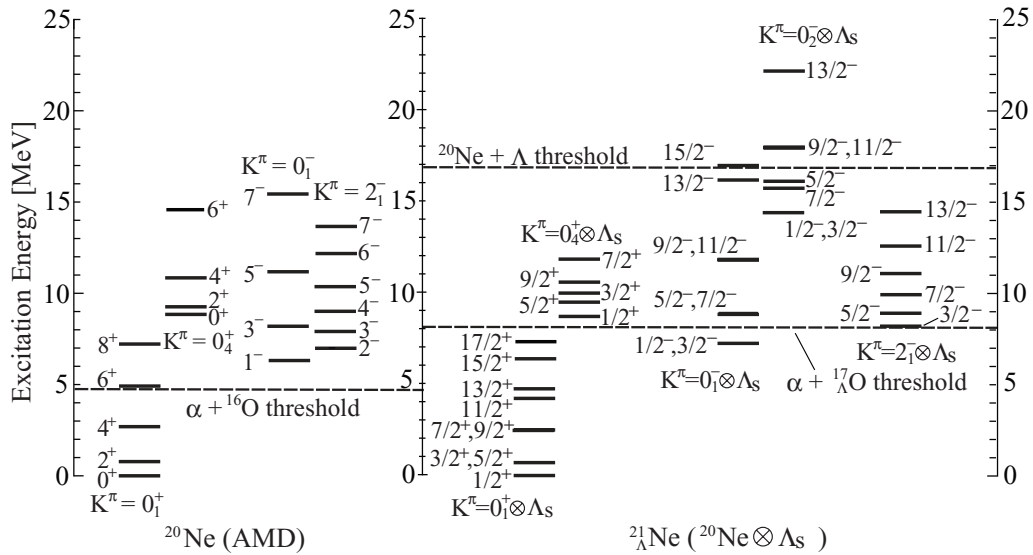
FIG. 3. Calculated low-lying energy spectra of $^{21}_{\Lambda}$Ne with a Λ_s are presented with that of ^{20}Ne.

$\alpha + {}^{17}_{\Lambda}$O threshold energies are also presented. The $\alpha + {}^{17}_{\Lambda}$O threshold is estimated by assuming that B_Λ of $^{17}_{\Lambda}$O is equal to that of $^{16}_{\Lambda}$O.

As seen in Fig. 3, Λ_s bounds two bands: the $0^+_1 \otimes \Lambda_s$ and $0^-_1 \otimes \Lambda_s$ bands. It should be noted that the unbound 1^-_1 state in ^{20}Ne goes below the α threshold and becomes bound. This is due to the attraction of the ΛN force. The binding of the 1^-_1 state by a Λ hyperon is also predicted in Ref. [16]. The $2^-_1 \otimes \Lambda_s$ band will also be bound, because the 2^-_1 is in the bound state in experiments while that obtained with AMD is unbound. The $0^-_2 \otimes \Lambda_s$ band is obtained as the solution of the GCM calculation. The corresponding band does not exist in ^{20}Ne. We think that this is due to the gluelike role of the Λ particle. It is also pointed out by Yamada *et al.* [16].

The hypernuclear states with Λ_p are shown in Fig. 4. We have obtained five bands: $0^+_1 \otimes \Lambda_p (0^+_1$ band with $\Lambda_p)$, $0^+_4 \otimes \Lambda_p$, $0^-_1 \otimes \Lambda_p$, $0^-_2 \otimes \Lambda_p$, and $2^-_1 \otimes \Lambda_p$. The band heads of the $0^+_1 \otimes \Lambda_p$ and $0^-_1 \otimes \Lambda_p$ bands lie below the ^{20}Ne $+ \Lambda$ threshold, but they are above the $\alpha + {}^{17}_{\Lambda}$O threshold. The presence of $0^+_1 \otimes \Lambda_p$ and $0^-_1 \otimes \Lambda_p$ bands have also been predicted by Ref. [16], and our calculation is consistent with its result.

2. Difference between shell and cluster bands in B_Λ and parity coupling

Here, we compare the Λ binding energies of the band head states of the $0^+_1 \otimes \Lambda_s$ and $0^-_1 \otimes \Lambda_s$ bands. As mentioned above, the mean-field-like and $\alpha + {}^{16}$O structures are mixed in the
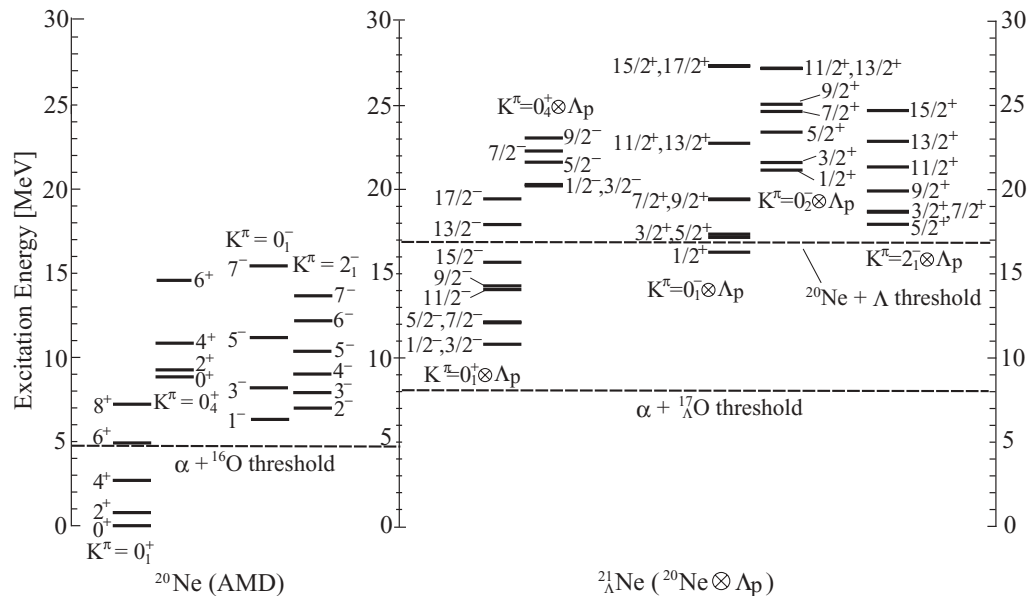
FIG. 4. Calculated low-lying energy spectra of $^{21}_{\Lambda}$Ne with a Λ_p are presented with that of ^{20}Ne.

TABLE I. Calculated energy E, excitation energy E_x, and Λ binding energy B_Λ for the band head states of the $0^+_1 \otimes \Lambda_s$ and $0^-_1 \otimes \Lambda_s$ bands are listed in MeV. The definition of B_Λ is given in Eq. (26). For comparison, theoretical and experimental E and E_x values of the 0^+_1 and 1^-_1 states in ^{20}Ne are also presented.

	Band	E	E_x	B_Λ
$^{21}_\Lambda$Ne(HyperAMD)	$(0^+_1 \otimes \Lambda_s)$	-176.5	0.0	16.9
$^{21}_\Lambda$Ne(HyperAMD)	$(0^-_1 \otimes \Lambda_s)$	-169.2	7.3	15.9
^{20}Ne(AMD)	$(K^\pi = 0^+_1)$	-159.6	0.0	–
^{20}Ne(AMD)	$(K^\pi = 0^-_1)$	-153.3	6.3	–
^{20}Ne(expt.)	$(K^\pi = 0^+_1)$	-160.6	0.0	–
^{20}Ne(expt.)	$(K^\pi = 0^-_1)$	-154.9	5.8	–

$K^\pi = 0^+_1$ band, while the $K^\pi = 0^-_1$ band has a pronounced $\alpha + {}^{16}$O cluster structure. In Table I, the total energy E, excitation energy E_x, and Λ binding energy B_Λ are listed. It shows that the Λ binding energy of the $0^+_1 \otimes \Lambda_s$ (ground) state is larger than that of the $0^-_1 \otimes \Lambda_s$ band head state. In Figs. 2(d)–2(f), the density distributions of the band head states of the $K^\pi = 0^+_1 \otimes \Lambda_s$ and $K^\pi = 0^-_1 \otimes \Lambda_s$ bands of $^{21}_\Lambda$Ne are presented. It is clearly seen that the Λ hyperon coupled to the $K^\pi = 0^-_1$ band head state of ^{20}Ne is localized around the ^{16}O cluster. This is because the single-particle potential of Λ_s is not parity symmetric due to the $\alpha + {}^{16}$O clustering and is deeper around the ^{16}O cluster. Indeed, B_Λ of $^{17}_\Lambda$O may be more than 12 MeV, while that of $^5_\Lambda$He is 2.6 MeV. On the other hand, the Λ hyperon coupled to the $K^\pi = 0^+_1$ band head state locates at the center of the ^{20}Ne nucleus and interacts with all nucleons. Therefore, the Λ_s in the $0^+_1 \otimes \Lambda_s$ band head state is more deeply bound than that in the $0^-_1 \otimes \Lambda_s$ band head state.

Since the Λ hyperon in the $0^-_1 \otimes \Lambda_s$ band locates around the ^{16}O cluster, it is not an eigenstate of parity of the single-particle state of Λ_s. Thus, the p-orbit component of the Λ hyperon should contribute to the $0^-_1 \otimes \Lambda_s$ state. Such mixed nature was called "parity coupling" in Ref. [16] for $^{21}_\Lambda$Ne or "intershell coupling" in Ref. [33]. It was argued that parity coupling could occur because the energy difference between the positive and negative parity states in the core nucleus is similar to that between the s and p orbits of the Λ hyperon [21]. However, in the present result, the parity coupling is due to the asymmetry of $\alpha + {}^{16}$O clustering. The $K^\pi = 0^+_1 \otimes \Lambda_p$ has a mixed configuration between the $K^\pi = 0^+_1 \otimes \Lambda_p$ and $0^-_1 \otimes \Lambda_s$ bands. We show the GCM amplitude of the $(1/2)^-$ state, which is the band head state of the $0^-_1 \otimes \Lambda_s$, in Fig. 5. The GCM amplitude is defined in Eq. (23), describing contributions from intrinsic wave functions to the GCM wave function. It shows that the contribution from the $0^+_1 \otimes \Lambda_p$ configuration is about 10%, while that from the $0^-_1 \otimes \Lambda_s$ configuration is about 90% at maximum. The opposite trend appears in the $0^-_1 \otimes \Lambda_s$ band.

Another interesting feature due to the parity coupling is the reduction of the level spacing. In Table III, the nuclear RMS radii for each state of ^{20}Ne and $^{21}_\Lambda$Ne are listed. It shows that the RMS radii decrease for the $K^\pi = 0^-_1 \otimes \Lambda_s$ band of $^{21}_\Lambda$Ne compared to the corresponding states of ^{20}Ne. However, as shown in Fig. 3, the level spacing between the $((1/2)^-, (3/2)^-)$ and $((5/2)^-, (7/2)^-)$ doublets of the $0^-_1 \otimes \Lambda_s$ band becomes smaller compared to that between 1^-_1 and 3^- states of ^{20}Ne. The parity coupling also causes the mixing of the nucleon part between the $K^\pi = 0^+_1$ and $K^\pi = 0^-_1$ bands in the $0^-_1 \otimes \Lambda_s$ band. Since the $K^\pi = 0^+_1$ band has a narrower level spacing, the level spacing of the $0^-_1 \otimes \Lambda_s$ band decreases by this mixing.

TABLE II. Intraband $B(E2)$ values (e^2 fm^4) for ^{20}Ne and $^{21}_\Lambda$Ne obtained by using AMD and compared with the $\alpha + {}^{16}$O $+\Lambda$ cluster model [16]. $cB(E2)$ represents the corrected $B(E2)$ values explained in the Appendix.

AMD					Yamada *et al.* [16]			
^{20}Ne		$^{21}_\Lambda$Ne			Changes	^{20}Ne		$^{21}_\Lambda$Ne	Changes
$K^\pi = 0^+_1$	$B(E2)$	$0^+_1 \otimes \Lambda_s$	$B(E2)$	$cB(E2)$	(%)	$K^\pi = 0^+_1$	$B(E2)$	$B(E2)$	(%)
$2^+ \to 0^+$	72.2	$(3/2)^+ \to (1/2)^+$	63.7	63.7	-11.8	$2^+ \to 0^+$	53.1	40.4	-23.9
		$(5/2)^+ \to (1/2)^+$	63.9	63.9	-11.5				
$4^+ \to 2^+$	86.9	$(7/2)^+ \to (3/2)^+$	64.3	71.4	-17.8	$4^+ \to 2^+$	67.2	52.0	-22.6
		$(9/2)^+ \to (5/2)^+$	75.7	75.7	-13.0				
$6^+ \to 4^+$	55.1	$(11/2)^+ \to (7/2)^+$	40.3	41.9	-23.9	$6^+ \to 4^+$	55.1	42.1	-23.6
		$(13/2)^+ \to (9/2)^+$	48.0	48.0	-12.9				
$8^+ \to 6^+$	17.0	$(15/2)^+ \to (11/2)^+$	15.9	16.2	-4.6	$8^+ \to 6^+$	29.0	23.0	-20.7
		$(17/2)^+ \to (13/2)^+$	17.1	17.1	0.8				

AMD					Yamada *et al.* [16]			
^{20}Ne		$^{21}_\Lambda$Ne			Changes	^{20}Ne		$^{21}_\Lambda$Ne	Changes
$K^\pi = 0^-_1$	$B(E2)$	$0^-_1 \otimes \Lambda_s$	$B(E2)$	$cB(E2)$	(%)	$K^\pi = 0^-_1$	$B(E2)$	$B(E2)$	(%)
$3^- \to 1^-$	221.2	$(5/2)^- \to (1/2)^-$	139.2	179.0	-19.1	$3^+ \to 1^+$	160.0	125.3	-21.7
		$(7/2)^- \to (3/2)^-$	178.5	178.5	-19.3				
$5^- \to 3^-$	249.3	$(9/2)^- \to (5/2)^-$	184.2	195.4	-21.6	$5^+ \to 3^+$	181.5	139.0	-23.4
		$(11/2)^- \to (7/2)^-$	189.3	189.3	-24.1				
$7^- \to 5^-$	240.3	$(13/2)^- \to (9/2)^-$	164.3	166.7	-30.6	$7^+ \to 5^+$	183.5	131.2	-28.5
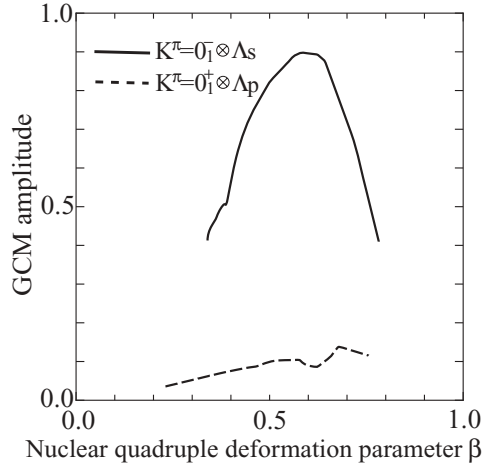
FIG. 5. GCM amplitude for the band head state $(1/2)^-$ of the $0_1^- \otimes \Lambda_s$ band. The definition of a GCM amplitude is given in Eq. (23). The solid line represents the contribution from the $0_1^- \otimes \Lambda_s$ band as a function of nuclear deformation parameter β. The dashed line shows that from the $0_1^+ \otimes \Lambda_p$ band.

3. Difference in B(E2) reduction

The difference in structure changes between the $0_1^+ \otimes \Lambda_s$ and $0_1^- \otimes \Lambda_s$ bands of $^{21}_\Lambda$Ne is clearly seen in the intraband

TABLE III. RMS radii (fm) for the $K^\pi = 0_1^+$, $K^\pi = 0_1^-$, and $K^\pi = 2_1^-$ bands of ^{20}Ne and its counterparts with Λ_s obtained by the present calculation. Δr_{RMS} is defined as a subtraction of RMS radii: $\Delta r_{RMS} = r_{RMS}(^{21}_\Lambda$Ne$) - r_{RMS}(^{20}Ne)$ for each corresponding state.

^{20}Ne		$^{21}_\Lambda$Ne		Δr_{RMS}
$K^\pi = 0_1^+$	r_{RMS}	$0_1^+ \otimes \Lambda_s$	r_{RMS}	
0^+	2.97	$(1/2)^+$	2.92	-0.05
2^+	2.96	$(3/2)^+$	2.91	-0.05
		$(5/2)^+$	2.91	-0.05
4^+	2.93	$(7/2)^+$	2.87	-0.06
		$(9/2)^+$	2.88	-0.04
6^+	2.87	$(11/2)^+$	2.81	-0.06
8^+	2.82	$(15/2)^+$	2.77	-0.04
^{20}Ne		$^{21}_\Lambda$Ne		Δr_{RMS}
$K^\pi = 0_1^-$	r_{RMS}	$0_1^- \otimes \Lambda_s$	r_{RMS}	
1^-	3.27	$(1/2)^-$	3.15	-0.11
		$(3/2)^-$	3.15	-0.11
3^-	3.24	$(5/2)^-$	3.13	-0.11
		$(7/2)^-$	3.14	-0.10
5^-	3.23	$(9/2)^-$	3.11	-0.12
		$(11/2)^-$	3.11	-0.13
7^-	3.23	$(13/2)^-$	3.06	-0.17
^{20}Ne		$^{21}_\Lambda$Ne		Δr_{RMS}
$K^\pi = 2_1^-$	r_{RMS}	$2_1^- \otimes \Lambda_s$	r_{RMS}	
2^-	2.98	$(3/2)^-$	2.93	-0.05
3^-	2.97	$(5/2)^-$	2.93	-0.04
4^-	2.96	$(7/2)^-$	2.91	-0.05
5^-	2.95	$(9/2)^-$	2.90	-0.05
6^-	2.94	$(11/2)^-$	2.89	-0.05

$B(E2)$ reduction. To compare $B(E2)$ values of $^{21}_\Lambda$Ne with those of ^{20}Ne, we corrected them under the assumption that a Λ hyperon occupies the s orbit for each hypernuclear state in the $0_1^+ \otimes \Lambda_s$ and $0_1^- \otimes \Lambda_s$ bands (see the Appendix). Both the bare and corrected $B(E2)$ values for the $0_1^+ \otimes \Lambda_s$ and $0_1^- \otimes \Lambda_s$ bands are presented in Table II. For comparison, $B(E2)$ values predicted by the cluster model calculation [16] are also listed in Table II.

A Λ hyperon causes $B(E2)$ reduction in the $0_1^- \otimes \Lambda_s$ and the $0_1^+ \otimes \Lambda_s$ bands. Indeed, Table II shows that the corrected $B(E2)$ values clearly decrease by adding a Λ hyperon in both the $0_1^+ \otimes \Lambda_s$ and the $0_1^- \otimes \Lambda_s$ bands. The $B(E2)$ reductions predicted by Yamada et al. [16] are more than 20% for those bands. However, in the present study, the corrected $B(E2)$ values for the $0_1^+ \otimes \Lambda_s$ band decrease less than 20%, while those for the $0_1^- \otimes \Lambda_s$ band are almost 20%, as shown in Table II. We consider the difference in the $B(E2)$ reduction mainly comes from the difference in the reduction of RMS radii between the $0_1^+ \otimes \Lambda_s$ and the $0_1^- \otimes \Lambda_s$ bands. The nuclear RMS radii for the $K^\pi = 0_1^+$, $K^\pi = 0_1^-$, and $K^\pi = 2_1^-$ bands of ^{20}Ne and for the corresponding bands with Λ_s are listed in Table III. The RMS radii for the $K^\pi = 0_1^-$ band change more than those of the $K^\pi = 0_1^+$ band. This is due to the difference in the clustering of these bands. Since the $K^\pi = 0_1^-$ band has well developed $\alpha + ^{16}$O cluster structure, a Λ hyperon reduces the intercluster distance, and it leads to the larger reduction of $B(E2)$ in the $K^\pi = 0_1^-$ band.

4. Level spacing of the ground band

The level spacing of the $0_1^+ \otimes \Lambda_s$ band becomes smaller compared to that of the $K^\pi = 0_1^+$ band of ^{20}Ne. We consider that it is due to the mixed nature of the $K^\pi = 0_1^+$ band of ^{20}Ne.

In the $K^\pi = 0_1^+$ band of ^{20}Ne, it has been discussed that the $\alpha + ^{16}$O cluster structure is broken at large angular momentum values [28,34]. In Fig. 6, the energy surfaces as a function of the nuclear deformation parameter β for the 0^+ and 8^+ states of the ^{20}Ne ground band and for its counterparts, the $(1/2)^+$ and $(15/2)^+$ states of the $^{21}_\Lambda$Ne ground band, are presented. The β at the energy minimum of each energy surface becomes smaller as angular momentum becomes larger. This is an indication of the brokenness of an $\alpha + ^{16}$O clustering.

We present the energy components for the $(1/2)^+$ and $(15/2)^+$ states of the ground band of $^{21}_\Lambda$Ne in Table IV. It shows that the 8^+ state gains the ΛN potential energy $V_{\Lambda N}$

TABLE IV. Energy E, nuclear energy E_N, expectation values of Λ kinetic energy T_Λ, and ΛN potential energy $V_{\Lambda N}$ for the $(1/2)^+$ and $(15/2)^+$ states of the $0_1^+ \otimes \Lambda_s$ band are presented. For comparison, E and E_N for the 0^+ and 8^+ states of ^{20}Ne are also presented.

	$^{21}_\Lambda$Ne$(0_1^+ \otimes \Lambda_s)$		^{20}Ne$(K^\pi = 0_1^+)$	
	$(1/2)^+$	$(15/2)^+$	0^+	8^+
E	-176.48	-170.08	-159.60	-152.40
E_N	-159.37	-152.19	-159.60	-152.40
T_Λ	7.72	8.06	–	–
$V_{\Lambda N}$	-24.83	-25.96	–	–
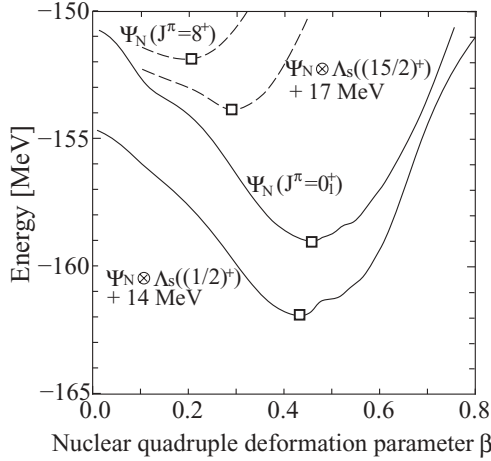
FIG. 6. Energy surface as function of nuclear deformation parameter β for the 0_1^+ (solid line) and the 8^+ (dashed line) states of the ^{20}Ne ground band and the corresponding states with Λ_s, $(1/2)^+$ and $(15/2)^+$, of $_{\Lambda}^{21}$Ne ground band are presented. The squares on each surface represent its minimum points. Note that the energy surfaces of the $(1/2)^+$ and the $(15/2)^+$ states are shifted by 14 and 17 MeV, respectively.

more than the 0^+ state, and then, the level spacing between the $(1/2)^+$ and $(15/2)^+$ states becomes smaller than that between 0^+ and 8^+ states. Here, as shown in Table III, the mean-field-like states at large momentum are more compact than the low-lying cluster states. Indeed, the RMS radius of the $(15/2)^+$ state is smaller than that of the $(1/2)^+$ state. Thus, ΛN potential energy increases in the $(15/2)^+$ state. Such a difference between the shell-model-like and cluster structures is predicted for $_{\Lambda}^{12}$C [35]. The same trend is seen in the $K^\pi = 0_1^- \otimes \Lambda_s$ band head states with well developed $\alpha + {}^{16}$O clustering and in the $K^\pi = 2_1^- \otimes \Lambda_s$ band with a deformed shell-model-like structure.

IV. SUMMARY

In this paper, we have applied HyperAMD to a $_{\Lambda}^{21}$Ne hypernucleus and investigated its structure. A Λ_s and Λ_p create five bands each and, thus, create a total of ten bands having not only an $\alpha + {}^{16}$O cluster but also a shell-model-like structure. Especially, the $0_1^+ \otimes \Lambda_s$, $0_1^- \otimes \Lambda_s$, and $2_1^- \otimes \Lambda_s$ bands are expected to bound.

The band head state of the $0_1^+ \otimes \Lambda_s$ band is the more deeply bound than that of the well-developed $\alpha + {}^{16}$O cluster band $0_1^- \otimes \Lambda_s$. This is because the Λ hyperon locates around the ^{16}O cluster in the $\alpha + {}^{16}$O state and bounds shallowly. At the same time, this shows the parity coupling between s and p orbits of the Λ hyperon. Indeed, the contribution from the later band is about 10% in the $0_1^- \otimes \Lambda_s$ band.

The intraband $B(E2)$ reduction by a Λ hyperon depends on the structure of the core states. The intraband $B(E2)$ reduction in the $0_1^- \otimes \Lambda_s$ band of $_{\Lambda}^{21}$Ne is larger than that in the $0_1^+ \otimes \Lambda_s$ band. This is mainly due to the reduction of the intercluster distance between α and ^{16}O clusters in the $K^\pi = 0_1^-$ band.

Other changes due to the coexistence of the cluster and shell-model-like aspects are found. The level spacing of the $0_1^+ \otimes \Lambda_s$ bands is smaller compared to the ground band in ^{20}Ne, while the nuclear RMS radii decrease for each state. It reflects the brokenness of the $\alpha + {}^{16}$O cluster at large angular momentum values. A Λ_s coupled to the larger angular momentum states is more bound than that coupled to the lower angular momentum states with the $\alpha + {}^{16}$O cluster structure.

APPENDIX: CORRECTION OF $B(E2)$ VALUES

We consider that the initial (final) state with angular momentum J_i (J_f) of a Λ hypernucleus consists of a core state with angular momentum j_i^C (j_f^C) and a Λ hyperon with $j^\Lambda = 1/2$. Thus,

$$|J_i\ M_i\rangle = \sum_{m_i^C, m_i^\Lambda} C_{m_i^C, m_i^\Lambda}^{J_i, M_i} |j_i^C\ m_i^C\rangle \otimes |j_i^\Lambda\ m_i^\Lambda\rangle,$$

$$|J_f\ M_f\rangle = \sum_{m_f^C, m_f^\Lambda} C_{m_f^C, m_f^\Lambda}^{J_f, M_f} |j_f^C\ m_f^C\rangle \otimes |j_f^\Lambda\ m_f^\Lambda\rangle,$$

where $C_{m_1, m_2}^{j_3, m_3} = \langle j_3 m_3 | j_1 m_1, j_2 m_2 \rangle$ is a Clebsch-Gorden coefficient. The $B(E2)$ of a Λ hypernucleus is calculated by the following:

$$B(E2, J_i \to J_f)$$
$$= \sum_{M_f} |\langle J_f\ M_f | \hat{O}(E2) | J_i\ M_i\rangle|^2$$
$$= \sum_{M_f} \left| \sum_{m_f^C, m_f^\Lambda} \sum_{m_i^C, m_i^\Lambda} C_{m_f^C, m_f^\Lambda}^{J_f, M_f} C_{m_i^C, m_i^\Lambda}^{J_i, M_i} \langle j_f^C\ m_f^C | \hat{O}(E2) | j_i^C\ m_i^C\rangle \right|^2$$
$$\times \delta_{m_f^\Lambda, m_i^\Lambda}.$$

By using the Wigner-Enckart theorem, we obtain

$$\langle j_f^C\ m_f^C | \hat{O}(E2) | j_i^C\ m_i^C\rangle = C_{m_i^C, m^{E2}}^{j_f^C, m_f^C} \langle j_f^C || \hat{O}(E2) || j_i^C\rangle,$$

where $\langle j_f^C || \hat{O}(E2) || j_i^C\rangle$ just depends on j_i^C and j_f^C. Finally, the $B(E2)$ is given as

$$B(E2, J_i \to J_f) = C \left| \langle j_f^C || \hat{O}(E2) || j_i^C\rangle \right|^2,$$

where

$$C = \sum_{M_f} \left(\sum_{m_f^C, m^\Lambda} \sum_{m_i^C, m^\Lambda} C_{m_f^C, m^\Lambda}^{J_f, M_f} C_{m_i^C, m^\Lambda}^{J_i, M_i} C_{m_i^C, m^{E2}}^{j_f^C, m_f^C} \right)^2,$$

$$m_i^\Lambda = m_f^\Lambda = m^\Lambda.$$

Finally, the corrected $B(E2)$ value $cB(E2)$ is obtained as

$$cB(E2, j_i^C \to j_f^C) = \frac{2j_f^C + 1}{2j_i^C + 1} |\langle j_f^C || \hat{O}(E2) || j_i^C\rangle|^2$$
$$= \frac{2j_f^C + 1}{2j_i^C + 1} \frac{B(E2, J_i \to J_f)}{C}.$$

[1] H. Bandō, Nucl. Phys. A **450**, 217c (1986).

[2] D. J. Millener, Nucl. Phys. A **691**, 93c (2001).

[3] K. Itonaga, T. Motoba, O. Richter, and M. Sotona, Phys. Rev. C **49**, 1045 (1994).

[4] T. Motoba, H. Bandō, and K. Ikeda, Prog. Theor. Phys. **70**, 189 (1983).

[5] T. Motoba, H. Bandō, K. Ikeda, and T. Yamada, Prog. Theor. Phys. Suppl. **81**, 42 (1985).

[6] R. H. Dalitz and A. Gal, Phys. Rev. Lett. **36**, 362 (1976).

[7] X.-R. Zhou, H.-J. Schulze, H. Sagawa, C.-X. Wu, and E.-G. Zhao, Phys. Rev. C **76**, 034312 (2007).

[8] M. T. Win and K. Hagino, Phys. Rev. C **78**, 054311 (2008).

[9] H.-J. Schulze, M. T. Win, K. Hagino, and H. Sagawa, Prog. Theor. Phys. **123**, 569 (2010).

[10] E. Hiyama, M. Kamimura, K. Miyazaki, and T. Motoba, Phys. Rev. C **59**, 2351 (1999).

[11] K. Tanida *et al.*, Phys. Rev. Lett. **86**, 1982 (2001).

[12] K. Ikeda *et al.*, Prog. Theor. Phys. Suppl. **52**, 1 (1972).

[13] K. Ikeda *et al.*, Prog. Theor. Phys. Suppl. **68**, 1 (1980).

[14] T. Sakuda and F. Nemoto, Prog. Theor. Phys. **62**, 1274 (1979).

[15] T. Sakuda and H. Bandō, Prog. Theor. Phys. **78**, 1317 (1987).

[16] T. Yamada, K. Ikeda, H. Bandō, and T. Motoba, Prog. Theor. Phys. **71**, 985 (1984).

[17] T. A. Rijken and Y. Yamamoto, Phys. Rev. C **73**, 044008 (2006).

[18] Y. Fujiwara, Y. Suzuki, and C. Nakamoto, Prog. Part. Nucl. Phys. **58**, 439 (2007).

[19] D. J. Millener, Nucl. Phys. A **804**, 84 (2008).

[20] D. J. Millener, A. Gal, C. Dover, and R. Dalitz, Phys. Rev. C **31**, 499 (1985).

[21] E. Hiyama and T. Yamada, Prog. Part. Nucl. Phys. **63**, 339 (2009).

[22] O. Hashimoto and H. Tamura, Prog. Part. Nucl. Phys. **57**, 564 (2006).

[23] Y. Yamamoto, T. Motoba, H. Himeno, K. Ikeda, and S. Nagata, Prog. Theor. Phys. Suppl. **117**, 361 (1994).

[24] Y. Kanada-En'yo, H. Horiuchi, and A. Ono, Phys. Rev. C **52**, 628 (1995).

[25] A. Doté, H. Horiuchi, and Y. Kanada-En'yo, Phys. Rev. C **56**, 1844 (1997).

[26] M. Kimura, Y. Sugawa, and H. Horiuchi, Prog. Theor. Phys. **106**, 1153 (2001).

[27] Y. Sugawa, M. Kimura, and H. Horiuchi, Prog. Theor. Phys. **106**, 1129 (2001).

[28] M. Kimura, Phys. Rev. C **69**, 044319 (2004).

[29] H. Matsumiya, K. Tsubakihara, M. Isaka, M. Kimura, A. Doté, and A. Ohnishi, Nucl. Phys. A **835**, 366 (2010); H. Matsumiya, K. Tsubakihara, M. Kimura, A. Dote, and A. Ohnishi, Phys. Rev. C **83**, 024312 (2011); M. Isaka, M. Kimura, A. Dote, and A. Ohnishi, *ibid.* **83**, 044323 (2011).

[30] J. Dechargé and D. Gogny, Phys. Rev. C **21**, 1568 (1980).

[31] T. Matsuse, M. Kamimura, and Y. Fukushima, Prog. Theor. Phys. **53**, 706 (1975).

[32] Y. Fujiwara, H. Horiuchi, and R. Tamagaki, Prog. Theor. Phys. **62**, 122 (1979).

[33] T. Motoba, Nucl. Phys. A **629**, 398c (1998).

[34] Y. Kanada-Enyo and H. Horiuchi, Prog. Theor. Phys. **93**, 115 (1995).

[35] E. Hiyama, M. Kamimura, T. Motoba, T. Yamada, and Y. Yamamoto, Phys. Rev. Lett. **85**, 270 (2000).